Coaxial electrospinning of WO3 nanotubes functionalized with bio-inspired Pd catalysts and their superior hydrogen sensing performance

Citation: Choi, Seon-Jin, Chattopadhyay, Saptarshi, Kim, Jae Jin, Kim, Sang-Joon, Tuller, Harry L., Rutledge, Gregory C., and Kim, Il-Doo. "Coaxial Electrospinning of WO3nanotubes Functionalized with Bio-Inspired Pd Catalysts and Their Superior Hydrogen Sensing Performance." Nanoscale 8, no. 17 (2016): 9159–9166. © 2015 Royal Society of Chemistry

As Published: http://dx.doi.org/10.1039/c5nr06611e

Publisher: Royal Society of Chemistry

Persistent URL: http://hdl.handle.net/1721.1/108045

Version: Author's final manuscript: final author's manuscript post peer review, without publisher's formatting or copy editing

Nanoscale

ARTICLE

Coaxial electrospinning of WO_3 nanotubes functionalized with bio-inspired Pd catalyst and their superior hydrogen sensing performance

Received 00th January 20xx,
Accepted 00th January 20xx

DOI: 10.1039/x0xx00000x

www.rsc.org/

Seon-Jin Choi,[a] Saptarshi Chattopadhyay,[b] Jae Jin Kim,[c] Sang-Joon Kim,[a] Harry L. Tuller,[c] Gregory C. Rutledge,[b,*] and Il-Doo Kim[a,*]

Macroporous WO_3 nanotubes (NTs) functionalized with nanoscale catalysts were fabricated using coaxial electrospinning combined with sacrificial templating and protein-encapsulated catalyst. The macroporous thin-walled nanotubular structures were obtained by introducing colloidal polystyrene (PS) particles to a shell solution of W precursor and poly(vinylpyrrolidone). After coaxial electrospinning with a core liquid of mineral oil and subsequent calcination, open pores with an average diameter of 173 nm were formed on the surface of WO_3 NTs due to decomposition of the PS colloids. In addition, catalytic Pd nanoparticles (NPs) were synthesized using bio-inspired protein cages, *i.e.*, apoferritin, and uniformly dispersed within the shell solution and subsequently on the WO_3 NTs. The resulting Pd-functionalized macroporous WO_3 NTs were demonstrated to be high performance hydrogen (H_2) sensors. In particular, Pd-funtionalized macroporous WO_3 NTs exhibited a very high H_2 response (R_{air}/R_{gas}) of 17.6 at 500 ppm with short response time. Furthermore, the NTs were shown to be highly selective for H_2 compared to other gases such as carbon monoxide (CO), ammonia (NH_3), and methane (CH_4). The results demonstrate a new synthetic method to prepare highly porous nanotubular structure with well-dispersed nanoscale catalysts, which can provide improved microstructures for chemical sensing.

Introduction

Hydrogen (H_2) has been regarded as a next generation fuel energy considering its abundance and high heat of combustion (142 kJ/g).[1, 2] In addition, burning of hydrogen produces only water, without harmful by-products, enabling environmentally friendly energy generation.[3, 4] However, there are several potential risks to be addressed prior to commercial use, such as the wide range of flammable concentration (4–75%), low ignition energy (0.02 mJ), high diffusion coefficient (0.61 cm^2/s), and large flame propagation velocity.[5-7] Moreover, hydrogen gas is colourless, odourless, and tasteless, which leads to difficulty in detection.[8] For these reasons, a highly sensitive hydrogen detector is required for safe storage and monitoring of hydrogen leakage.

Semiconductor metal oxides (SMOs) have been studied as promising gas sensors, considering their low cost, fast response, stability, and high reactivity toward analyte gases.[9] Recently, advances in nanostructure synthetic methods have promoted the development of highly sensitive and selective gas sensors having large surface area and porosity.[10, 11] Among the various approaches, electrospinning is a facile and versatile method to obtain one-dimensional (1D) SMO nanostructures with large surface-to-volume ratio and high porosity, adequate for high performance hydrogen sensors.[12, 13] A templating route combined with electrospinning has been suggested as a powerful strategy to obtain porous nanostructures.[14] For example, hollow nanotubular structures were demonstrated using electrospun polymeric composite nanofibers (NFs) by coating a thin inorganic layer, such as Al_2O_3,[15] NiO,[16] WO_3,[17, 18] and ZnO,[19] and subsequent high-temperature calcination to decompose the inner polymeric component and crystallize the outer inorganic layer. In addition, polymeric colloids were introduced into the electrospinning solution to form pores on SMO NFs.[20-22] It was shown that pore diameter and distribution on the SMO surface can be controlled by introducing different sizes of the colloid templates.

Coaxial (or two-fluid) electrospinning has been proposed as an effective method to fabricate hollow nanotubular structure that eliminates the additional synthesis processes such as coating of inorganic layer on the sacrificial templates.[13, 23-26] A variety of inorganic nanotubes (NTs) were obtained using coaxial electrospinning, including TiO_2,[27, 28] α-Fe_2O_3,[29] and SnO_2[30] for specific applications. However, to the best of our knowledge, coaxial electrospinning combined with sacrificial templating to synthesize macroporous SMO NTs has not yet been demonstrated. The macroporous SMO NTs are advantageous, considering that gas molecules can more

[a] Department of Material Science and Engineering, Korea Advanced Institute of Science and Technology (KAIST), Daejeon 305–701, Republic of Korea. E-mail: idkim@kaist.ac.kr; Fax: +82-42-350-5329; Tel: +82-42-350-3329
[b] Department of Chemical Engineering, Massachusetts Institute of Technology, 77 Massachusetts Avenue, Cambridge, MA 02139, USA. E-mail: rutledge@mit.edu; Fax: +1-617-324-3127; Tel: +1-617-253-0171
[c] Department of Materials Science and Engineering, Massachusetts Institute of Technology, 77 Massachusetts Avenue, Cambridge, MA 02139, USA.

Electronic Supplementary Information (ESI) available: Coaxial electrospinning with different feeding rates, additional TEM analysis for pore size analysis, TEM and EDS analysis of Rh-loaded macroporous WO_3 NTs, and dynamic response transition poperties of sensors. See DOI: 10.1039/x0xx00000x

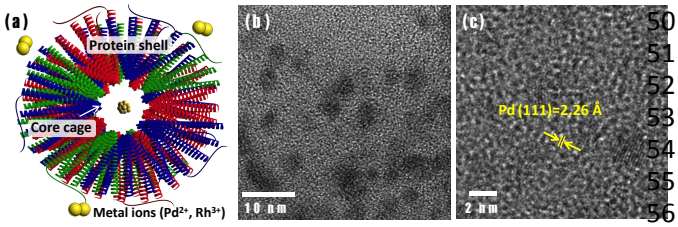

Fig. 1 (a) Schematic illustration of apoferritin protein cage for nanocatalyst synthesis, TEM image of (b) apoferritin-encapsulated Pd nanoparticles (AF-Pd NPs), and (c) high-resolution TEM (HR-TEM) image AF-Pd NPs.

effectively diffuse into the core of the SMO NTs, thereby promoting gas reactions on the inner surface.

Catalytic functionalization of SMO-based materials enhances sensitivity and selectivity of gas sensors. Noble metallic nanoparticles (NPs) such as Pt,[31] Pd,[32] and Rh[33, 34] are known to be the most effective catalysts for high performance gas sensors. To have maximum catalytic effect, the diameters of the catalytic NPs should be on the order of a few nanometers.[35] Moreover, uniform dispersion of the NPs is desirable; otherwise, the sensing performance degrades rapidly due to the agglomeration of catalytic NPs.[36, 37]

In this work, we propose a method to fabricate nanocatalyst-loaded macroporous WO_3 NTs using coaxial electrospinning combined with sacrificial templating and bio-inspired catalyst functionalization. Multiple pores were formed on the thin-walled WO_3 NTs after subsequent calcination at high temperature. In addition, well-dispersed catalyst functionalization was achieved by introducing protein-encapsulated metallic NPs to the shell solution during coaxial electrospinning. The main focus of this research was to examine a new synthetic method to obtain macroporous nanotubular SMO structures with functionalization by well-distributed nanocatalysts, and to demonstrate the remarkably improved hydrogen sensing performances resulting therefrom.

Experimental section

Materials

Ammonium metatungstate hydrate $[(NH_4)_6H_2W_{12}O_{40}{\cdot}xH_2O]$, polyvinylpyrrolidone (PVP, M_w=1,300,000 g/mol), potassium tetrachloropalladate(II) (K_2PdCl_4), sodium borohydride ($NaBH_4$), heavy mineral oil, and 0.2 μm filtered apoferritin from equine spleen were purchased from Sigma-Aldrich (St. Louis, USA). Polystyrene (PS) latex microspheres with the average diameter of 200 nm dispersed at 2.5 wt% in water were purchased from Alfa Aesar (Ward Hill, USA). All chemicals were used without further purification.

Synthesis of nanocatalyst particles encapsulated by protein cages

To synthesize well-dispersed and nanoscale catalyst particles, we employed bio-inspired protein cages, *i.e.*, apoferritin, that consisted of a 24-subunit protein complex that exhibits a hollow spherical structure (Fig. 1a). These protein cages can encapsulate metal ions, and the subsequent reduction process can produce protein-encapsulated metallic NPs.[38] Firstly, 1 g of apoferritin solution was mixed with 0.1 M NaOH solution to control pH of the solution around 8.6. Then, 1.8 wt % of Pd precursor (K_2PdCl_4) aqueous solution was added to the apoferritin solution and gently stirred at 100 rpm using a magnetic bar to penetrate Pd^{2+} ions into the inner cavity of apoferritin. After stirring for 1 h, a reducing agent of $NaBH_4$ (1 M) was rapidly injected into the solution to form metallic Pd NPs encapsulated by apoferritin (hereafter, apoferritin-encapsulated Pd NPs are referred as AF-Pd NPs). Finally, the prepared AF-Pd NPs were centrifuged at 12,000 rpm for 10 min to remove the remaining Pd^{2+}, and subsequently re-dispersed in DI water.

Synthesis of Pd-loaded macroporous WO_3 NTs

Hollow WO_3 nanotubular structure was synthesized by the coaxial electrospinning approach as illustrated in Fig. 2a. Different electrospinning solutions were emitted through the coaxial nozzle (SKU BCN-0802, Inovenso^{TM}) having different diameters, *i.e.*, core diameter of 0.8 mm and shell diameter of 1.6 mm, with concentric configuration. Mineral oil was utilized as a core electrospinning solution due to its easy vaporization at high-temperature. For the shell solution, 0.2 g of ammonium metatungstate hydrate and 0.25 g of PVP were dissolved in 1.5 g of DI water containing 2.5 wt% PS colloids and continuously stirred at room temperature for 3 h. For catalyst functionalization, the prepared AF-Pd NPs were separately introduced in the shell electrospinning solution with the concentrations of 0.1 wt%.

The resulting solutions were electrospun at feeding rates of 10 μL/min of mineral oil for the core and 30–100 μL/min of composite solution for the shell, using syringe pumps. A constant DC voltage of 30 kV was applied between the coaxial nozzle and aluminum foil, employed as collector. The distance between the nozzle and the collector was 15 cm. The as-spun core/shell composite NFs were obtained after coaxial electrospinning (Fig. 2b). The shell layer comprised apoferritin-encapsulated catalytic NPs and W precursor/PVP composite decorated with PS colloids. For the core fluid, mineral oil was used. The as-spun core/shell composite NFs were calcined at 600 ˚C for 1 h in ambient air to obtain catalyst-loaded macroporous WO_3 NTs having multiple, approximately circular pores on the thin wall of NTs (Fig. 2c). Dense WO_3 NTs without PS colloid templates and pristine macroporous WO_3 NTs without catalyst functionalization were synthesized as well, for comparison.

Characterization of H_2 sensing performances

All of the sensors were stabilized in air for 24 h as baseline before the measurement. The sensors were exposed to different analytes (hydrogen, carbon monoxide, ammonia, and methane) with concentrations ranging from 10 ppm to 500 ppm. Each analyte was exposed for 10 min, followed by 10 min of exposure to air to recover the initial baseline values. The resistance changes were measured using a data acquisition system (34970A, Hewlett-Packard), and the sensors were characterized by their relative response (R_{air}/R_{gas}), where R_{air} is the baseline resistance of the sensor upon exposure to air and R_{gas} is the resistance measured upon exposure to a particular

analyte. The operating temperatures of the sensors were controlled to be 450 ˚C in a furnace tube.

Results and discussion

Morphological and structural evaluation

The microstructures of the protein-encapsulated catalytic Pd NPs were examined using TEM (Fig. 1b and c). It was clearly observed that well-dispersed NPs were synthesized within the protein cages. The good dispersion can be explained by electrostatic repulsion between the protein templates due to surface charge, which prevented agglomeration between the NPs. In addition, the overall size of the protein cage was 12–13 nm, whereas the inner cavity size was 7–8 nm.[39] The inner cavity size limited the size of the nanoscale particles to diameters less than 8 nm. As confirmed by TEM analysis, the synthesized AF-Pd NPs showed average diameters of 2 nm (Fig. 1b). Moreover, the Pd NPs were observed to be crystalline with the crystal planes of Pd (111), corresponding to the interplanar distances of 2.26, in evidence (Fig. 1c).

The AF-Pd NPs were dispersed in the shell electrospinning solutions for the catalytic functionalization. Core/shell composite NFs decorated with PS colloid templates and apoferritin-encapsulated catalytic NPs were achieved after electrospinning (Fig. 2b). Polymeric components, mineral oil, and protein cages were decomposed during subsequent calcination of the as-spun core/shell composite NFs, while forming WO_3 NTs by oxidation of the W precursor (Fig. 2c). SEM observation revealed the rugged surface morphology of the as-spun core/shell composite NFs due to the decoration of PS colloids on the surface (Fig. 2d). Different microstructures were obtained after calcination at 600 ˚C, depending on the feeding rate of shell solution (f_s) with the fixed core solution feeding rate (f_c=10 μL/min) (Supporting Information, Fig. S1). When the shell feeding rate was slow, *i.e.*, f_s=30 μL/min, an open tubular structure was formed due to the limited coating of shell composite solution on mineral oil. On the other hand, perfect tubular structures were achieved when f_s was 80 μL/min or 100 μL/min. Fig. 2e shows the macroporous WO_3 NTs with multiple pores on the surface when f_s and f_c were 100 μL/min and 10 μL/min, respectively. The pore sizes were evaluated by TEM, and the average diameter was 173 nm (Supporting Information, Fig. S2). The decreased average pore diameter as comparing with the original diameter (*i.e.*, 200 nm) of the PS colloid was mainly attributed to the shrinkage of the spherical PS colloids during the thermal decomposition and the migration of W precursor in the early stage of heat treatment.[20]

The microstructures of the catalytic Pd-loaded macroporous WO_3 NTs were investigated (Fig. 2f). The surface morphologies of the Pd-loaded macroporous WO_3 NTs were maintained, with only minor differences when compared to the pristine macroporous WO_3 NTs. In addition, close observation

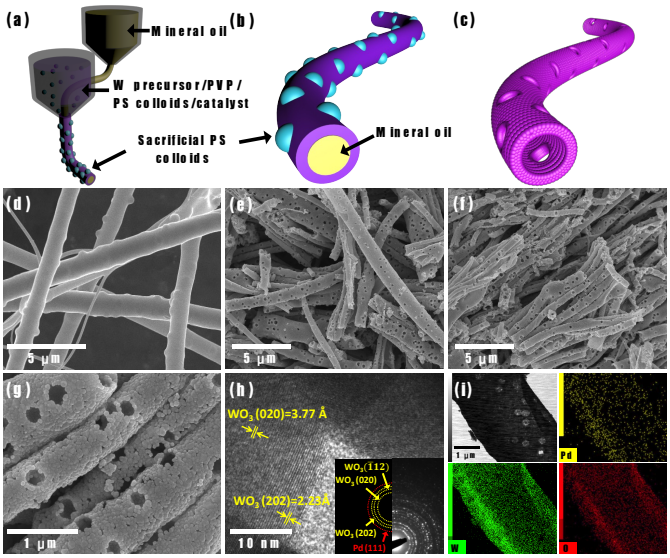

Fig. 2 Schematic illustrations of (a) coaxial electrospinning using mineral oil in the core and composite solution in the shell, (b) as-spun W precursor/PVP composite nanotubes (NTs) decorated with PS colloid templates and apoferritin-encapsulated nanocatalysts, and (c) catalyst-loaded macroporous WO_3 NTs with multiple pores after calcination at 600 °C for 1 h. SEM images of (d) as-spun W precursor/PVP composite NTs decorated with PS colloid templates, (e) macroporous WO_3 NTs, (f) Pd-loaded macroporous WO_3 NTs, and (g) magnified SEM image of (f) after calcination. (h) HR-TEM image with selected area electron diffraction (SAED) pattern in the inset and (i) scanning TEM image with energy dispersive X-ray spectroscopy (EDS) mapping images of Pd-loaded macroporous WO_3 NTs.

of Pd-loaded macroporous WO_3 NTs exhibited approximately circular pores on the surface (Fig. 2g). High-resolution TEM (HR-TEM) observation of Pd-loaded macroporous WO_3 NTs revealed the polycrystalline WO_3 structures with crystal planes of (020) and (202), which corresponds to inter-planar distances of 3.77 Å and 2.23 Å (Fig. 2h). Selected area electron diffraction (SAED) patterns of Pd-loaded macroporous WO_3 NTs presented WO_3(020), $WO_3(\bar{1}12)$, and WO_3(202) crystal planes, with inter-planar distances of 3.77 Å, 3.12 Å, and 2.62 Å, respectively, which are partially investigated in HR-TEM analysis (in the inset of Fig. 2h). However, crystal planes and SAED pattern of Pd NPs were not clearly observed due to the low content of Pd in WO_3 NTs. To confirm the Pd component and the distribution, energy dispersive X-ray spectroscopy (EDS) analysis was carried out. The result clearly revealed uniform distribution of Pd over the WO_3 NTs (Fig. 2i). In addition, a scanning TEM image also showed the hollow structure of Pd-loaded macroporous WO_3 NTs (Fig. 2i). To further confirm the chemical state of Pd, X-ray photoelectron spectroscopy (XPS) analysis was performed (Fig. S3). Even though the intensities of Pd peaks were very weak due to the low concentration of Pd in the WO_3 NTs, high-resolution XPS peaks at the vicinity of Pd 3*d* are mainly originated by the oxidized state of Pd, i.e., Pd^{2+}(PdO) with binding energies of 336.9 eV and 342.2 eV for $3d_{5/2}$ and $3d_{3/2}$, respectively.[40]

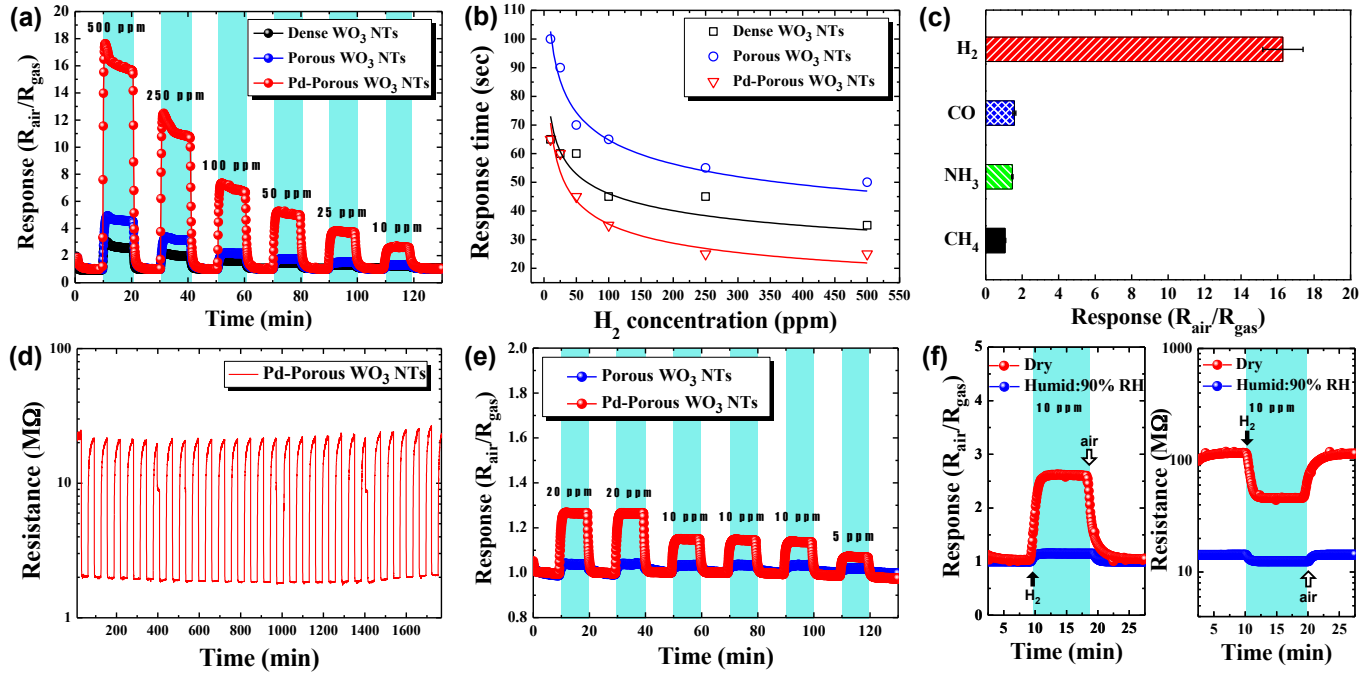

Fig. 3 (a) Dynamic response transition and (b) response time property of dense WO_3 NTs, porous WO_3 NTs, and Pd-Porous WO_3 NTs in the gas concentration range of 10–500 ppm at 450 °C. (c) Selective H_2 sensing property of Pd-Porous WO_3 NTs against other analytes with the gas concentration of 500 ppm at 450 °C. (d) Cyclic resistance transition of Pd-Porous WO_3 NTs toward H_2 with the gas concentration of 500 ppm at 450 °C. (e) Dynamic response transition of porous WO_3 NTs and Pd-Porous WO_3 NTs in the gas concentration range of 5–20 ppm in air at high relative humidity (90% RH) at 450 °C. (f) Dynamic response and resistance transition properties of Pd-Porous WO_3 NTs to 10 ppm of H_2 in dry and humid air at 450 °C.

Hydrogen molecule sensing characterization

To demonstrate the superior H_2 sensing performance of the Pd-loaded macroporous WO_3 NTs, gas sensing characteristics were evaluated using dense WO_3 NTs, macroporous WO_3 NTs (Porous WO_3 NTs), and Pd-loaded macroporous WO_3 NTs (Pd-Porous WO_3 NTs) in the gas concentration range of 10–500 ppm at 450 °C (Fig. 3). Dynamic response measurements showed that an approximately 1.6-fold improvement in the response was observed with the porous WO_3 NTs (R_{air}/R_{gas}=4.9) compared to the response of dense WO_3 NTs (R_{air}/R_{gas}=3). In addition, a dramatically improved H_2 response of 17.6 was obtained with Pd-Porous WO_3 NTs at 500 ppm which was 5.9- and 3.6-fold better than that observed with dense WO_3 NTs and porous WO_3 NTs, respectively. Furthermore, Pd-Porous WO_3 NTs exhibited outstanding response (R_{air}/R_{gas}=2.6) at a very low concentration of 10 ppm (Supporting Information, Fig. S4).

Response time characteristic of the sensors were investigated at different concentrations (Fig. 3b). The response time is defined as the elapsed time to reach 90% saturation of maximum response. The Pd-loaded macroporous WO_3 NTs showed fast response due to the catalytic effect inducing active surface reactions. Very fast response within 25 sec was achieved with Pd-Porous WO_3 NTs at 500 ppm of H_2. However, relatively slow response times with dense WO_3 NTs (35 sec) and porous WO_3 NTs (50 sec) were observed at the same concentration. Particularly, the porous WO_3 NTs showed much longer response times than the dense WO_3 NTs. This can be attributed to the fact that the porous WO_3 NTs had more available surface reaction sites as a result of the formation of open pores, which accounted for the longer response time as well as the slightly improved response compared to the dense WO_3 NTs. In addition, it should be noted that all the sensors showed longer response times at low H_2 concentration. The observation of longer response times with decreasing gas concentrations has been reported previously.[41-43] The reaction is basically diffusion-limited at low H_2 concentration. Based on the theoretical study, the response time transition can be explained by a non-linear diffusion reaction model.[44] In that study, the diffusion time (τ) was defined by

$$\tau = k \cdot x_0^2 \cdot C_0^{r-1}/D \quad (1)$$

where, k, x_0, C_0, and D are the reaction rate constant, film thickness, gas concentration, and diffusion coefficient, respectively. The constant r was found to be in the range of 0.3–1. In the present study, our sensor exhibited the constant r in the range of 0.7–0.8 as indicated by fitting of eqn (1) to the data in Fig. 3b. The model is based on the dependence of response time on gas concentration. Specifically, the response time is determined by a non-linear adsorption isotherm, which leads to a concentration-dependent response time.

Selectivity of H_2 detection with respect to other, potentially interfering gases such as carbon monoxide (CO), ammonia (NH_3), and methane (CH_4) at 500 ppm was investigated using Pd-Porous WO_3 NTs (Fig. 3c). The results revealed that Pd-Porous WO_3 NTs showed remarkably high H_2 response (R_{air}/R_{gas}=16.3±1.1) with minor responses (R_{air}/R_{gas}<1.6)

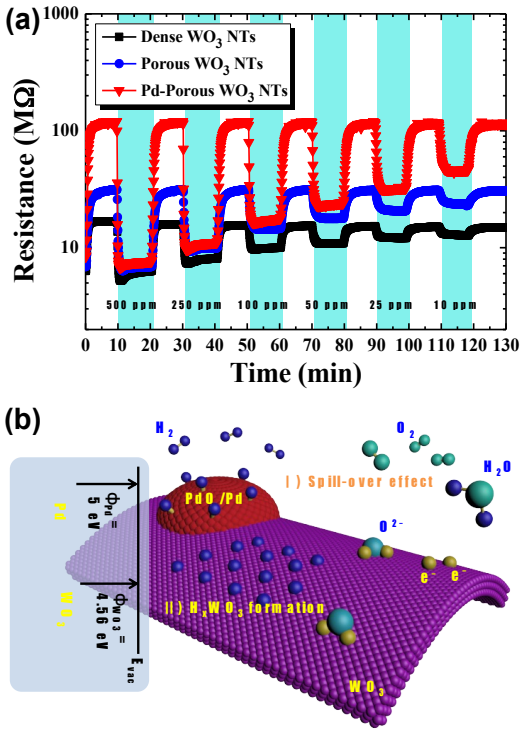

Fig. 4 (a) Dynamic resistance changes of dense WO_3 NTs, porous WO_3 NTs, and Pd-Porous WO_3 NTs toward H_2 within the concentration range of 10–500 ppm at 450 °C. (b) Schematic illustration of H_2 sensing mechanism of Pd-Porous WO_3 NTs.

toward the other gases, which confirms the high H_2 selectivity of these materials. Stable H_2 sensing property of Pd-Porous WO_3 NTs was evaluated as well by cyclic exposure of H_2 (Fig. 3d). The sensor showed stable resistance changes over 25 cycles toward 500 ppm of H_2.

The effect of moisture on the H_2 sensing property was investigated using the porous WO_3 NTs and Pd-Porous WO_3 NTs in the concentration range of 5–20 ppm in air with high relative humidity (90% RH) at 450 °C (Fig. 3e). Under these conditions, the Pd-Porous WO_3 NTs exhibited a response of 1.26 at 20 ppm, which is a 20% improvement in response compared to that of pristine porous WO_3 NTs. However, dramatically decreased response characteristics were observed in both Pd-Porous WO_3 NTs and pristine porous WO_3 NTs under the high humidity conditions. A reduction in response of approximately 90% was observed for Pd-Porous WO_3 NTs at 10 ppm of H_2 in humid air (Fig. 3f). The relatively insensitive H_2 response of Pd-Porous WO_3 NTs in humid air is mainly attributed to the formation of hydroxyl groups (–OH) on the surface of WO_3 NTs.[55] As a result, decreased baseline resistance was also observed with Pd-Porous WO_3 NTs in humid air (Fig. 3f).

Hydrogen sensing mechanism

The mechanism responsible for the improved H_2 sensing performance of the Pd-Porous WO_3 NTs was investigated (Fig. 4). Changes in the dynamic resistance of the sensors with respect to changes in H_2 concentrations were evaluated by comparing the baseline resistances and resistance changes (Fig. 4a). All the sensors exhibited decreasing resistance when the sensors were exposed to H_2 gas. A well-known explanation for the decreasing resistance attributes the decrease to the elimination of chemisorbed oxygen species, *i.e.*, O^-, O^{2-}, and O_2^-, by the reaction with H_2 on the surface of WO_3. When n-type WO_3 is stabilized in ambient air, oxygen species are chemisorbed on the surface of WO_3, withdrawing electrons from the conduction band to provide the baseline resistance. Then, upon exposure to H_2 gas, the resistance decreases as H_2 reacts with the chemisorbed oxygen species, thereby donating

Table 1. Comparison of important parameters for H_2 sensors

Composites	Sensing type	Response definition	Sensitivity (Response)	Detection limit	Selectivity	Response / recovery time	Operating Temp.	Ref.
Pd-WO_3 nanotubes	**Resistivity**	**R_{air}/R_{gas}**	**17.6 @ 500 ppm**	**10 ppm**	**CH_4, CO, NH_3**	**25 sec/-**	**450 °C**	**This work**
Pd-WO_3 nanoplates	Resistivity	R_{air}/R_{gas}	843 @ 0.3 vol%	0.1 vol%	CH_4, C_3H_6O, C_2H_6, C_3H_8O, NH_3	~50 sec/ ~25 sec	80 °C	45
Pd-WO_3 nanoplates	Conductivity	R_{air}/R_{gas}	34 @ 0.1 vol%	0.05 %	-	24 sec/-	Room Temp.	46
Pd-WO_3 nanolamellae	Resistivity	R_{air}/R_{gas}	~6×10^3 @ 400 ppm	200 ppm	-	-/-	250 °C	47
Pd/WO_3 film	Resistivity	$(R_0 - R_{H2})/R_{H2}$	4.77×10^4 @ 2%	500 ppm	-	-/ 47 sec	80 °C	48
Pd-WO_3 thick film	Resistivity	$(R_{air} - R_{gas})/R_{gas}$	69 @ 200 ppm	50 ppm	-	<5 min/-	180 °C	49
Pd-WO_3 nanowire	Resistivity	R_{air}/R_{gas}	3.1 @ 1000 ppm	1000 ppm	C_3H_6O, CH_4O, C_3H_8O	76 sec/ 2491 sec	300 °C	50
Pd-WO_3 film (Pd/W=10%)	Voltage change	$(V_{gas} - V_{air})/V_{air}$	2.5×10^4 @ 1300 ppm	1300 ppm	-	~100 sec/ ~4000 sec	Room Temp.	51
Pd-WO_3 film	Conductivity	$(I_{gas}/I_{air}) - 1$	400 @ 2300 ppm	2300 ppm	CH_4	102 sec/ 7 sec	350 °C	52
Pd-WO_3 film	Resistivity	$(R_0 - R_{H2})/R_{H2}$	1200 @ 3000 ppm	4 ppm	CH_4O, C_2H_6O, C_3H_6O, C_3H_8O, CH_2O	1400 sec/-	Room Temp.	53
Pd-WO_3 nanowire	Conductivity	$(G - G_0)/(G_0 \cdot c) \times 100\%$	~1000 @ 1000 ppm	10 ppm	NO, H_2S, CO	-/ <900 sec	130 °C	54

electrons back to the conduction band.

Comparing the baseline resistances, pristine porous WO_3 NTs exhibited slightly higher resistance (31.5 MΩ) than that of dense WO_3 NTs (16.7 MΩ), which was mainly attributed to the macroporous structure of the former. In the case of Pd-Porous WO_3 NTs, there was huge increase in baseline resistance (1196 MΩ) compared to the other sensors. The increased baseline resistance can be explained by the formation of a Schottky barrier between Pd and WO_3 (Fig. 4b). The different work functions of Pd (ϕ=5 eV)[56] and WO_3 (ϕ=4.56 eV)[20] can form an electron depletion layer at the interface, which results in the increase in baseline resistance. In addition, formation of a p-n junction can increase the baseline resistance. In other words, Pd can be slightly oxidized to form p-type PdO on the surface of Pd due to the high-temperature calcination in ambient air.[32] The formation of a p-n junction can also expand the electron depletion layer at the interface, thereby increasing baseline resistance.

The reaction mechanisms responsible for the large resistance changes of Pd-Porous WO_3 NTs toward H_2 are discussed next. As shown in the schematic illustration in Fig. 4b, two reactions are mainly affected by the catalytic Pd. Generally, Pd can dissociate H_2 molecules into H atoms (H_{ads}) on the surface of Pd NP. These H atoms are distributed onto the WO_3 surface, which is known as the 'spill-over effect', to react with chemisorbed oxygen species (i.e., O^{2-} and O^-), resulting in the production of H_2O molecules as expressed in the following reactions.[57, 58]

$$2H_{ads} + O^{2-} \rightarrow H_2O + 2e^- \quad (2)$$

$$2H_{ads} + O^- \rightarrow H_2O + e^- \quad (3)$$

The other reaction path is the formation of hydrogen tungsten bronzes (H_xWO_3) on the surface of WO_3 NTs by the partial reduction of WO_3, as described below.[45]

$$xH_{ads} + WO_3 \rightarrow H_xWO_3 \quad (4)$$

The hydrogen atoms serve as electron donors, thereby increasing the free carriers in WO_3 and decreasing the overall resistance of Pd-Porous WO_3 NTs.[46] Therefore, these two reaction paths are believed to be responsible for the large decrease in resistance from the baseline, and for the strong response of Pd-Porous WO_3 NTs toward H_2.

It has been demonstrated that Pd-WO_3 composites are outstanding sensing materials for H_2 detection. Table 1 summarizes recent publications on Pd-WO_3 composite sensing layers for H_2 detection. A majority of the previous studies were performed in the form of a thin film structure, whereas a few works demonstrate the superior H_2 sensing properties using nanostructures. Regardless, the present work shows a relatively strong response (R_{air}/R_{gas}=17.6) at a relatively low H_2 concentrations, compared to the previous studies. In addition, we demonstrated the lowest limit of detection (10 ppm) with very fast responding speed (25 sec).

Conclusions

In this work, we have demonstrated the use of coaxial electrospinning combined with sacrificial templating to produce macroporous semiconductor metal oxide (SMO) nanostructures. During the coaxial electrospinning, PS colloids were introduced to the electrospinning solution to serve as templates for macropores on the surface of the WO_3 NTs. Circular-shaped pores with an average diameter of 173 nm were achieved on the WO_3 NTs after subsequent calcination. The apoferrtin protein cage is shown to be a powerful agent for distributing nanocatalyst uniformly on SMO sensing layers. The noble metallic Pd NPs were synthesized using apoferritin protein cages and thus distributed on the macroporous WO_3 NTs during coaxial electrospinning. The Pd-loaded macroporous WO_3 NTs exhibited very fast response times, which is mainly attributed to the catalytic effect of Pd. Particularly, Pd-loaded macroporous WO_3 NTs showed high sensitivity and selectivity toward H_2. Very high response (R_{air}/R_{gas}) of 17.6 was achieved at 500 ppm of H_2. In addition, Pd-loaded macroporous WO_3 NTs revealed high H_2 selectivity with minor responses toward potential interfering gases such as CO, NH_3, and CH_4. This work provides a novel synthetic method using two-fluid electrospinning for macroporous WO_3 NTs with bio-inspired nanocatalyst for high performance chemical sensors.

Acknowledgements

This work was supported by the Center for Integrated Smart Sensors funded by the Ministry of Science, ICT & Future Planning as Global Frontier Project (CISS-2011-0031870) and partially funded by Intel's University Research Office (URO). We also would like to acknowledge the Institute for Soldier Nanotechnology at MIT for use of facilities

Notes and references

1. P. A. Russo, N. Donato, S. G. Leonardi, S. Baek, D. E. Conte, G. Neri and N. Pinna, *Angew. Chem. Int. Edit.*, 2012, **51**, 11053-11057.
2. T. Hubert, L. Boon-Brett, G. Black and U. Banach, *Sens. Actuators B*, 2011, **157**, 329-352.
3. M. Z. Ahmad, V. B. Golovko, R. H. Adnan, F. Abu Bakar, J. Y. Ruzicka, D. P. Anderson, G. G. Andersson and W. Wlodarski, *Int. J. Hydrogen Energ.*, 2013, **38**, 12865-12877.
4. S. K. Arya, S. Krishnan, H. Silva, S. Jean and S. Bhansali, *Analyst*, 2012, **137**, 2743-2756.
5. N. H. Al-Hardan, M. J. Abdullah and A. A. Aziz, *Int. J. Hydrogen Energ.*, 2010, **35**, 4428-4434.
6. E. Sennik, Z. Colak, N. Kilinc and Z. Z. Ozturk, *Int. J. Hydrogen Energ.*, 2010, **35**, 4420-4427.
7. S. Sumida, S. Okazaki, S. Asakura, H. Nakagawa, H. Murayama and T. Hasegawa, *Sens. Actuators B*, 2005, **108**, 508-514.
8. T. Samerjai, N. Tamaekong, C. Liewhiran, A. Wisitsoraat, A. Tuantranont and S. Phanichphant, *Sens. Actuators B*, 2011, **157**, 290-297.
9. I. D. Kim, A. Rothschild and H. L. Tuller, *Acta Mater.*, 2013, **61**, 974-1000.
10. T. Wagner, S. Haffer, C. Weinberger, D. Klaus and M. Tiemann, *Chem. Soc. Rev.*, 2013, **42**, 4036-4053.
11. D. J. Wales, J. Grand, V. P. Ting, R. D. Burke, K. J. Edler, C. R. Bowen, S. Mintova and A. D. Burrows, *Chem. Soc. Rev.*, 2015, **44**, 4290-4321.
12. B. Ding, M. R. Wang, X. F. Wang, J. Y. Yu and G. Sun, *Mater. Today*, 2010, **13**, 16-27.
13. A. Greiner and J. H. Wendorff, *Angew. Chem. Int. Edit.*, 2007, **46**, 5670-5703.
14. H. Y. Chen, J. C. Di, N. Wang, H. Dong, J. Wu, Y. Zhao, J. H. Yu and L. Jiang, *Small*, 2011, **7**, 1779-1783.

15. Q. Peng, X. Y. Sun, J. C. Spagnola, G. K. Hyde, R. J. Spontak and G. N. Parsons, *Nano Lett.*, 2007, **7**, 719-722.
16. N. G. Cho, H. S. Woo, J. H. Lee and I. D. Kim, *Chem. Commun.*, 2011, **47**, 11300-11302.
17. S. J. Choi, F. Fuchs, R. Demadrille, B. Grevin, B. H. Jang, S. J. Lee, H. Lee, H. L. Tuller and I. D. Kim, *ACS Appl. Mater. & Interfaces*, 2014, **6**, 9061-9070.
18. S. J. Choi, I. Lee, B. H. Jang, D. Y. Youn, W. H. Ryu, C. O. Park and I. D. Kim, *Anal. Chem.*, 2013, **85**, 1792-1796.
19. S. H. Choi, G. Ankonina, D. Y. Youn, S. G. Oh, J. M. Hong, A. Rothschild and I. D. Kim, *ACS Nano*, 2009, **3**, 2623-2631.
20. S. J. Choi, C. Choi, S. J. Kim, H. J. Cho, M. Hakim, S. Jeon and I. D. Kim, *Sci. Rep.*, 2015, **5**, 8067.
21. S. J. Choi, S. J. Kim, W. T. Koo, H. J. Cho and I. D. Kim, *Chem. Commun.*, 2015, **51**, 2609-2612.
22. S. J. Choi, C. Choi, S. J. Kim, H. J. Cho, S. Jeon and I. D. Kim, *RSC Adv.*, 2015, **5**, 7584-7588.
23. H. L. Qu, S. Y. Wei and Z. H. Guo, *J. Mater. Chem. A*, 2013, **1**, 11513-11528.
24. D. Li and Y. N. Xia, *Nano Lett.*, 2004, **4**, 933-938.
25. J. H. Yu, S. V. Fridrikh and G. C. Rutledge, *Adv. Mater.*, 2004, **16**, 1562-1566.
26. Z. C. Sun, E. Zussman, A. L. Yarin, J. H. Wendorff and A. Greiner, *Adv. Mater.*, 2003, **15**, 1929-1932.
27. X. Zhang, V. Aravindan, P. S. Kumar, H. Liu, J. Sundaramurthy, S. Ramakrishna and S. Madhavi, *Nanoscale*, 2013, **5**, 5973-5980.
28. X. Zhang, V. Thavasi, S. G. Mhaisalkar and S. Ramakrishna, *Nanoscale*, 2012, **4**, 1707-1716.
29. S. Chaudhari and M. Srinivasan, *J Mater Chem*, 2012, **22**, 23049-23056.
30. J. Cao, T. Zhang, F. Li, H. Yang and S. Liu, *New. J. Chem.*, 2013, **37**, 2031-2036.
31. J. Shin, S. J. Choi, I. Lee, D. Y. Youn, C. O. Park, J. H. Lee, H. L. Tuller and I. D. Kim, *Adv. Funct. Mater.*, 2013, **23**, 2357-2367.
32. D. J. Yang, I. Kamienchick, D. Y. Youn, A. Rothschild and I. D. Kim, *Adv. Funct. Mater.*, 2010, **20**, 4258-4264.
33. K. I. Choi, S. J. Hwang, Z. F. Dai, Y. C. Kang and J. H. Lee, *RSC Adv.*, 2014, **4**, 53130-53136.
34. S. J. Kim, I. S. Hwang, C. W. Na, I. D. Kim, Y. C. Kang and J. H. Lee, *J. Mater. Chem.*, 2011, **21**, 18560-18567.
35. N. Ma, K. Suematsu, M. Yuasa and K. Shimanoe, *ACS Appl. Mater. & Interfaces*, 2015, **7**, 15618-15625.
36. S. Vallejos, T. Stoycheva, P. Umek, C. Navio, R. Snyders, C. Bittencourt, E. Llobet, C. Blackman, S. Moniz and X. Correig, *Chem. Commun.*, 2011, **47**, 565-567.
37. I. S. Hwang, J. K. Choi, H. S. Woo, S. J. Kim, S. Y. Jung, T. Y. Seong, I. D. Kim and J. H. Lee, *ACS Appl. Mater. & Interfaces*, 2011, **3**, 3140-3145.
38. J. Jang, S. Kim, S.-J. Choi, N.-H. Kim, H. Meggie, A. Rothschild and I.-D. Kim, *Nanoscale*, 2015, **7**, 16417.
39. Z. Heger, S. Skalickova, O. Zitka, V. Adam and R. Kizek, *Nanomedicine*, 2014, **9**, 2233-2245.
40. N. H. Kim, S. J. Choi, D. J. Yang, J. Bae, J. Park and I. D. Kim, *Sens. Actuators B*, 2014, **193**, 574-581.
41. V. N. Mishra and R. P. Agarwal, *Microelectr. J.*, 1998, **29**, 861-874.
42. H. R. Kim, K. I. Choi, J. H. Lee and S. A. Akbar, *Sens. Actuators B*, 2009, **136**, 138-143.
43. E. Rossinyol, A. Prim, E. Pellicer, J. Arbiol, F. Hernandez -Ramirez, F. Peiro, A. Cornet, J. R. Morante, L. A. Solovyov, B. Z. Tian, T. Bo and D. Y. Zhao, *Adv. Funct. Mater.*, 2007, **17**, 1801-1806.
44. J. W. Gardner, *Sens. Actuators B*, 1990, **1**, 166-170.
45. Y. R. Wang, B. Liu, S. H. Xiao, H. Li, L. L. Wang, D. P. Cai, D. D. Wang, Y. Liu, Q. H. Li and T. H. Wang, *J. Mater. Chem. A*, 2015, **3**, 1317-1324.
46. B. Liu, D. P. Cai, Y. Liu, D. D. Wang, L. L. Wang, Y. R. Wang, H. Li, Q. H. Li and T. H. Wang, *Sens. Actuators B*, 2014, **193**, 28-34.
47. Z. Q. Hua, M. Yuasa, T. Kida, N. Yamazoe and K. Shimanoe, *Thin Solid Films*, 2013, **548**, 677-682.
48. M. Zhao, J. Huang and C.-W. Ong, *Int. J. Hydrogen. Energ.*, 2013, **38**, 15559-15566.
49. A. Boudiba, C. Zhang, P. Umek, C. Bittencourt, R. Snyders, M. G. Olivier and M. Debliquy, *Int. J. Hydrogen. Energ.*, 2013, **38**, 2565-2577.
50. F. Chavez, G. F. Perez-Sanchez, O. Goiz, P. Zaca-Moran, R. Pena-Sierra, A. Morales-Acevedo, C. Felipe and M. Soledad-Priego, *Appl. Surf. Sci.*, 2013, **275**, 28-35.
51. S. Fardindoost, A. I. Zad, F. Rahimi and R. Ghasempour, *Int. J. Hydrogen Energ.*, 2010, **35**, 854-860.
52. E. Ghadiri, A. Iraji zad and F. Razi, *Synth. React. Inorg. M*, 2007, **37**, 453-456.
53. M. Zhao, J. X. Huang and C. W. Ong, *Nanotechnology*, 2012, **23**, 315503.
54. J. Kukkola, M. Mohl, A. R. Leino, J. Maklin, N. Halonen, A. Shchukarev, Z. Konya, H. Jantunen and K. Kordas, *Sens. Actuators B*, 2013, **186**, 90-95.
55. H. Li, B. Liu, D. P. Cai, Y. R. Wang, Y. Liu, L. Mei, L. L. Wang, D. D. Wang, Q. H. Li and T. H. Wang, *J. Mater. Chem. A*, 2014, **2**, 6854-6862.
56. J. H. Ahn, J. Yun, Y. K. Choi and I. Park, *Appl. Phys. Lett.*, 2014, **104**, 013508.
57. Z. Y. Zhang, X. M. Zou, L. Xu, L. Liao, W. Liu, J. Ho, X. H. Xiao, C. Z. Jiang and J. C. Li, *Nanoscale*, 2015, **7**, 10078-10084.
58. X. W. Li, Y. Liu, J. C. Hemminger and R. M. Penner, *ACS Nano*, 2015, **9**, 3215-3225.